
Reinforcement Learning for Chemical Ordering in Alloy Nanoparticles

Jonas Elsborg^{1,2} Emma L. Hovmand¹ Arghya Bhowmik^{1,2*}

¹Department of Energy Conversion and Storage,
Technical University of Denmark, Kongens Lyngby 2800, Denmark

²CAPeX Pioneer Center for Accelerating P2X Materials Discovery,
Technical University of Denmark, Kongens Lyngby 2800, Denmark

Abstract

We approach the search for optimal element ordering in bimetallic alloy nanoparticles (NPs) as a reinforcement learning (RL) problem and have built an RL agent that learns to perform such global optimization using the geometric graph representation of the NPs. To demonstrate the effectiveness, we train an RL agent to perform composition-conserving atomic swap actions on the icosahedral nanoparticle structure. Trained once on randomized $\text{Ag}_x\text{Au}_{309-x}$ compositions and orderings, the agent discovers previously established ground state structure. We show that this optimization is robust to differently ordered initialisations of the same NP compositions. We also demonstrate that a trained policy can extrapolate effectively to NPs of unseen size. However, the efficacy is limited when multiple alloying elements are involved. Our results demonstrate that RL with pre-trained equivariant graph encodings can navigate combinatorial ordering spaces at the nanoparticle scale, and offer a transferable optimization strategy with the potential to generalize across composition and reduce repeated individual search cost.

Keywords: reinforcement learning, global structure optimization, chemical ordering, alloy nanoparticle, graph neural network

1 Introduction

Metallic nanoparticles (NPs) are widely used as heterogeneous (electro)catalysts because their high site-to-volume ratios and tunable active sites enable exceptional reactivity [1, 2]. The elemental composition, size, shape, and atomic ordering of NPs directly influence their catalytic properties and stability by determining the distribution and nature of active sites on the surface [3]. Determining the atomic structure of NPs is therefore a central objective in designing efficient and selective catalysts, and several computational strategies have been developed to resolve their ground-state atomic arrangements [3]. However, NP structure search faces two central challenges: the high cost of evaluating the total energy of a given atomic structure/ordering to assess its stability, and the limited efficiency of algorithms for exploring the structure/ordering space using this energy evaluator. As a result, most NP structure searches rely on inexpensive classical potentials [4–6], while first-principles Density Functional Theory (DFT) is generally too computationally expensive to use in the search itself and is instead reserved for validating a limited set of candidate structures [5, 7]. Recently, machine learning (ML) potentials have been used to accelerate the energy evaluation step while retaining near-DFT accuracy in energetics [8–10]. The search space for possible atomic configurations grows combinatorially with cluster size, and constructing effective search algorithms is equally crucial and can be paired with all different energy evaluation methods. Mixed-integer

*Corresponding author: arbh@dtu.dk

programming (MIP) [11], Monte Carlo (MC) sampling [12–14], and basin hopping (BH) [15–18] techniques have been used to determine provably optimal structures (within the accuracy of the energy/fitness function). Genetic algorithms (GAs) explore the vast combinatorial configuration space by iteratively evolving a population of candidate structures, and are generally more efficient and popular [3–5, 8, 19–26]. For each GA run, one must evaluate the fitness (energy) of many candidates over numerous generations. However, GA and other classical methods like MC are intractable for larger systems, and a significant drawback from these methods is the non-transferability and lack of generalization across different compositions, forcing independent optimization runs for each elemental composition or NP size separately.

Starting from seminal work by Hammer et al. using image based reinforcement learning (RL) [27–31], recent work has turned to RL as a unified optimization approach for atomic structures [29, 32]. An RL agent can be trained to construct molecules or nanoparticle structures atom-by-atom [30, 31, 33, 34], or even fragment-by-fragment [35]. Another approach is to train RL agents to modify an existing structure by treating the configuration space as a labelled graph, which the RL agent learns to reconfigure [36]. The benefit of a trained RL policy is that it can rapidly propose near-optimal configurations without performing an exhaustive search from scratch for each structure or composition. So far, this approach has been explored only for nanoparticles with small number of atoms [32, 34]. In this work, we built and deployed a reinforcement learning framework that couples an equivariant encoder [37] with a reinforcement learning model trained via proximal policy optimization (PPO) to perform composition-preserving structure manipulation actions on the atomic graph to optimize ordering. Trained once, the agent reproduces a set of provably exact ground state orderings of Mackay-icosahedral $\text{Ag}_x\text{Au}_{309-x}$ nanoparticles.

2 Methods

2.1 Nanoparticle optimisation as a reinforcement learning problem

We formulate the search for a minimum-energy nanoparticle structure as a sequential decision-making task, i.e., a Markov Decision Process (MDP). In this MDP, a state s_t represents an atomic configuration of a NP (positions and types of all atoms) at time step t in the MDP. In our setting, an action a_t at time t corresponds to a modification of the NP structure resulting from swapping the positions $\mathbf{x}_A = (x_A, y_A, z_A)$ and $\mathbf{x}_B = (x_B, y_B, z_B)$ of two atoms A and B. The environment computes the potential energy of the resulting structure and returns a reward $r_t = E(s_t) - E(s_{t+1})$ based on the energy change between the energy of the pre-swap state, $E(s_t)$, and that of the post-swap state, $E(s_{t+1})$. After each action, we also perform a local geometry relaxation.

Thus, if $r_t > 0$, the atomic swap resulted in a lower-energy state at $t + 1$ than at t . This approach incentivises the agent to move toward more stable configurations. It also fully satisfies the Markov property (the energy outcome depends only on the current atomic arrangement) and provides a dense scalar reward. Maximising the return G , i.e. the cumulative reward, over a horizon of H actions corresponds to minimising the NP’s energy. This results in a sum that signals the overall energy difference between the initial state and the final state (assuming no discount factor is used, see Appendix A.1). The formulation allows the agent to explore the configurational space in a guided manner since it learns a policy that, at each step, chooses how to alter the NP to reach a lower-energy state at the end. By maximising G , the agent can discover non-trivial sequences of modifications that yield large net energy drops, even if some intermediate steps may lead to an increase in energy. This ability of RL to handle long-term credit assignment (assigning credit to actions that lead to benefits much later) is a key advantage in navigating complex energy landscapes with many local minima.

Recent studies have demonstrated that policy-based RL agents can efficiently navigate such energy landscapes to find stable, low-energy structures of molecules, metal clusters and bulk materials [33–36]. To evaluate the energy of NPs, we use the Effective Medium Theory (EMT) potential - a semi-empirical many-body potential [38]. Even though EMT has relatively cheap energy evaluations, the search for global minima can be very expensive as the number of chemical orderings grows combinatorially. For a fixed shape with N sites and bimetallic composition A_xB_{N-x} , the labellings scale as $\binom{N}{x}$. For example, in a 309-atom icosahedral NP ($\text{Ag}_x\text{Au}_{309-x}$) with elemental composition of $\text{Ag}_{162}\text{Au}_{147}$, we get $\binom{309}{162} \approx 3.3 \times 10^{91}$ chemical orderings, and symmetry reduces this only by a modest constant factor [24].

2.2 RL Algorithm: Actor–Critic with PPO and KL Regularisation

We adopt an actor–critic version of the proximal policy optimisation algorithm [39] (PPO) to train the agent’s policy. The actor is the policy $\pi_{\theta}(a | s)$, parametrised by weights θ , used to predict a distribution over actions a_t given state s_t at time t . The critic is a value function $V_{\phi}(s_t)$, with parameters ϕ , and it estimates the expected cumulative reward (proportional to the expected energy reduction) from s_t . By teaching the critic to predict the state values, the actor can learn to select actions that yield high returns as judged by the critic’s feedback. We use generalised advantage estimation [40] (GAE) to compute the advantage of an action a_t compared to default behaviour (expectation under the value function). All algorithm details are in Appendix A.

Due to our definition of MDP as a sequence of atomic swap actions, we define a single atom swap action as the choice of an atom pair $a_t = (i_t, j_t)$. Thus, at each time step t , the agent picks an *anchor* atom i which is then paired with a suitable *partner* atom indexed by j (Figure 1).

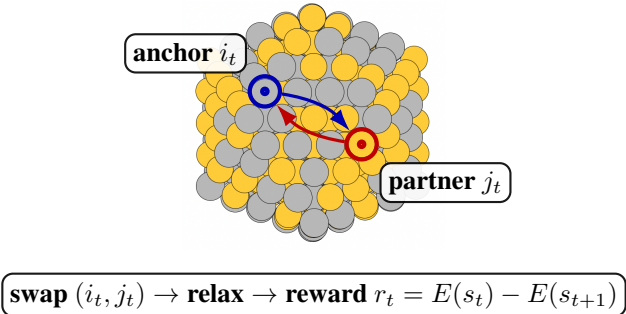


Figure 1: Agent–environment step on the Ag/Au NP: highlight the chosen **anchor** i and **partner** j , swap species, relax, compute reward, and continue. In Figure 8 in Appendix C, we show snapshots from a full episode of anchor-partner swaps for a trained model.

We use a factorized actor which acts on features distilled from a frozen ORB-v3 atomic graph encoder [37]. We use two neural network policy heads:

$$\pi_{\theta}(a_t | s_t) = \pi_{\theta_a}(i_t | s_t) \pi_{\theta_p}(j_t | s_t, i_t), \quad \theta = (\theta_a, \theta_p), \quad (1)$$

where θ_a are the features of the *anchor* policy neural network, and θ_p are the features of the *partner* policy neural network, which is conditioned on the chosen anchor atom indexed by i_t (See Appendix A.2 for details on how these policy networks are constructed).

3 Experimental Results

Icosahedral NPs are used here to demonstrate the effectiveness of the proposed learning framework. Catalytic alloy NPs are often icosahedral, which are interesting due to the presence of a high density of edges/vertices, creating strained, low-coordination sites that can strongly modulate reaction intermediate adsorption energies. The discrete “magic-number” shells (N=13, 55, 147, 309, 561,...) also promote composition-dependent surface segregation and core–shell ordering, phenomena directly linked to catalytic selectivity and activity, and thus are critical to resolve accurately [41]. As a testbed for our model, icosahedra are ideal: they have clear, well-studied ground-state motifs, yet they have an enormous configuration space with many energetically near-degenerate arrangements [42–44]. This creates a challenging test case, and effective policies must both discover the right shell assignments and avoid combinatorial traps. Their standardized sizes let us probe generalization across composition with controlled geometry and later test size generalization.

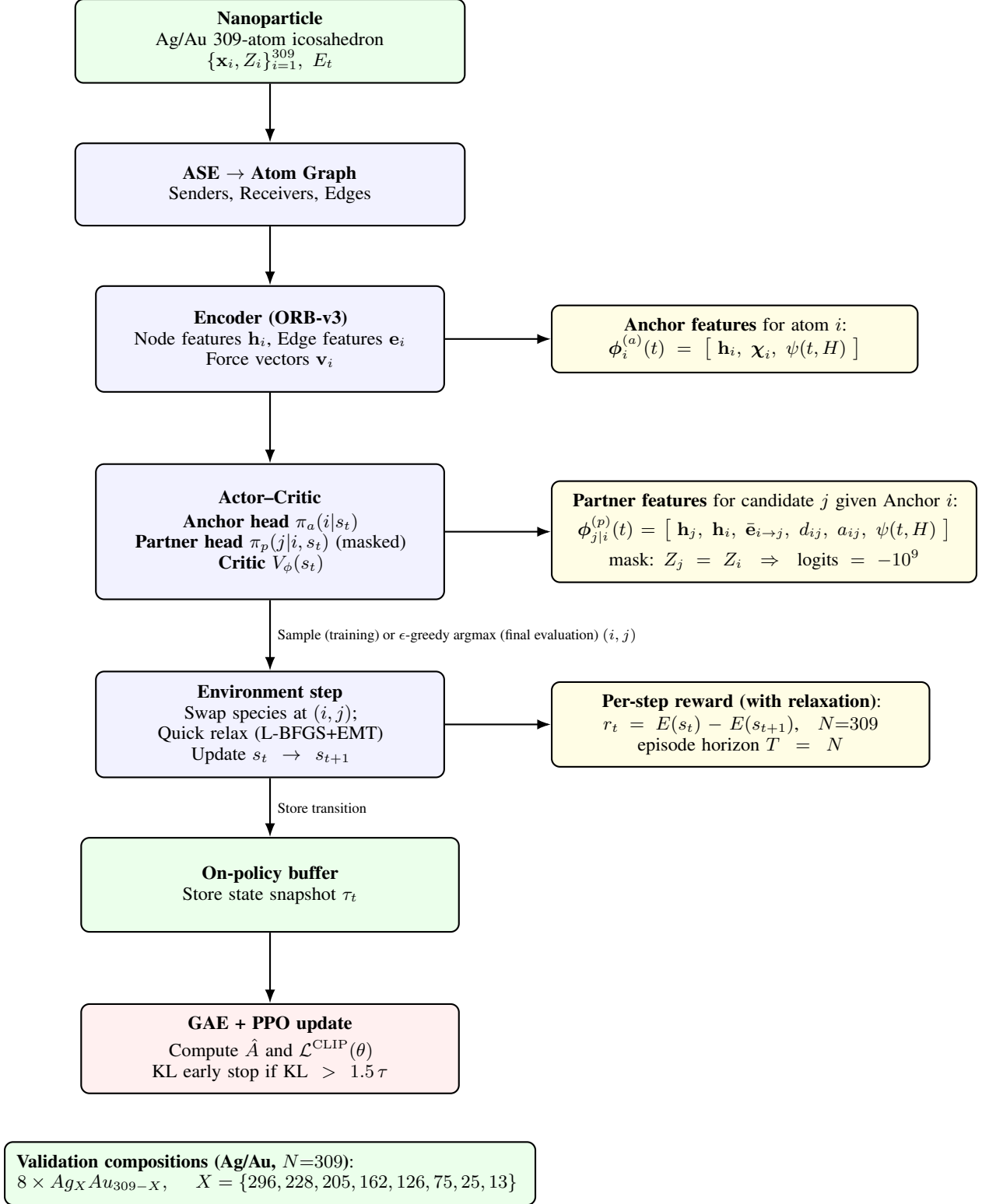


Figure 2: PPO implementation and model flow for the proposed composition generalized model for global nanoparticle atomic ordering optimization.

Testing For final testing of the generalized agent, we treat the provably lowest energy structures with respect to the EMT potential established with MIP solutions of $\text{Ag}_X \text{Au}_{309-X}$ icosahedral nanoparticles

of Larsen et al. [11] as reference targets, and use eight compositions whose ground state orderings were specifically reported there. At the end of training, each GPU samples a randomized configuration of these formulas, and the agent is tasked with solving these structures to find the minimum energy using an evaluation horizon $H_{eval} = 2 \times N_{atoms} = 618$.

In Figure 3, we show the single ordering (out of 8 - one for each GPU) found for each composition, which had the lowest final energy.

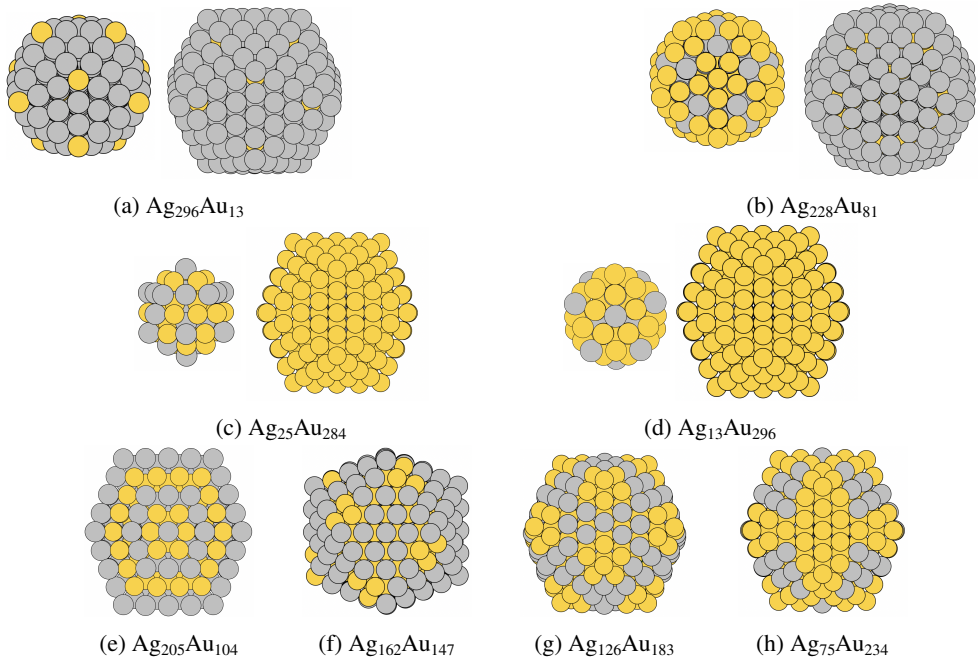


Figure 3: Lowest energy structures found by the trained agent for (a)-(h) the eight test compositions. For the first four (a)-(d) both the internal core structure (left) and outside shell structure (right) are provided.

3.1 Optimiser policy can generalise across composition (Experiment-1)

Current state-of-the-art models require running the ordering search individually from scratch for each elemental composition for an NP motif. A significant breakthrough could be achieved by learning a policy that generalizes across elemental compositions.

Training To evaluate composition generalisation of the model, we trained for 100 epochs \times 300 episodes on 309-atom icosahedra with fully randomised $\text{Ag}_X\text{Au}_{309-X}$ compositions and orderings (no ordering repeats). Training uses eight 24 GB RTX 3090 GPUs, each sampling distinct nanoparticles (varied by ordering and elemental composition) per episode. The horizon is $H_{train} = 309$, and for each step, the agent selects an anchor-partner pair, swaps them, relaxes the structure, and receives a reward $r_t = E(s_t) - E(s_{t+1})$. Because all states are similarly relaxed, r_t reflects only ordering improvements. We optimise actor-critic networks with PPO + GAE while keeping the ORB-v3 encoder frozen (Figure 2, see Appendix A for further details). We show training curves in Figure 6 in Appendix B.

Results For the structures dominated by a single species in Figures 3a-3d, we show both an interior view in the left figures and an exterior view of the shell in the right figures. For structures dominated by Ag (Figures 3a and 3b), the agent prefers an Ag-shell with Au atoms placed either at the subsurface corners (Figure 3a) or at the subsurface edges (Figure 3b). These structures are the same as the ground state structures found by Larsen et al. [11]. For structures dominated by Au (Figures 3c and 3d), the agent prefers an Au-shell with Ag atoms placed in the innermost 3 shells, with no Ag atoms in shells 4 and 5. The patterns of these structures are also similar to those found in Larsen et al. [11], except for a few atoms. However, the agent correctly places an Ag atom in the centre of

these nanoparticles (in fact, all nanoparticles have a correctly placed central atom). For the more balanced compositions of Figures 3e-3h, the agent finds the same structures as those in Larsen et al. [11], including the perfectly ordered "onion-shell" structure for $\text{Ag}_{205}\text{Au}_{104}$. The agent also finds the correct "flower-like" surface decoration of $\text{Ag}_{126}\text{Au}_{183}$ (Figure 3g), as well as the $\text{Ag}_{162}\text{Au}_{147}$ surface decoration with 3-atom clusters of Au (Figure 3f), and the $\text{Ag}_{75}\text{Au}_{234}$ surface decoration with 6-atom clusters of Ag (Figure 3h). These results affirm the suitability of our model towards generalization across the chemical composition of a particular-sized icosahedral NP, lowering the cost of atomic ordering search through amortization.

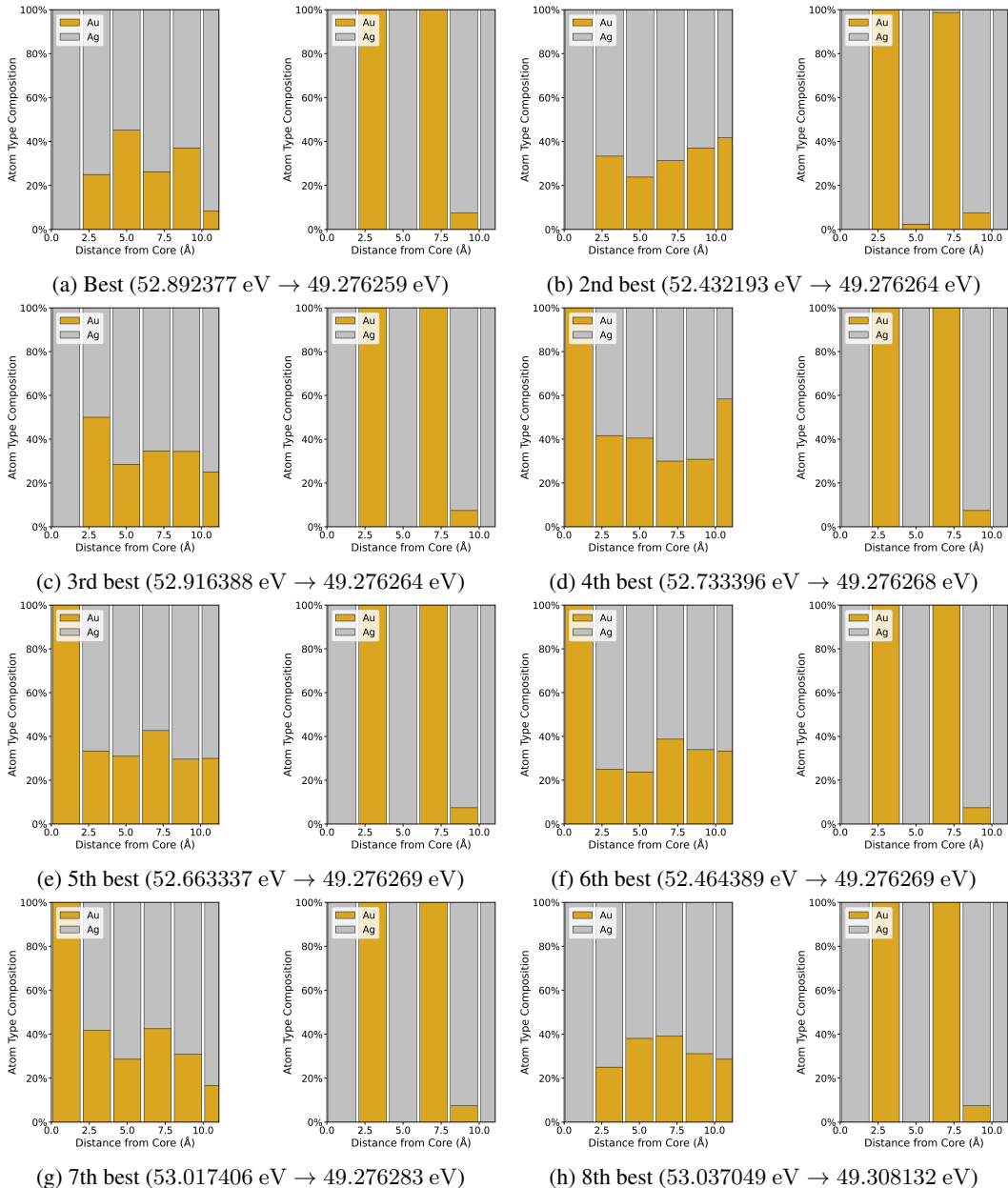


Figure 4: Elemental radial distribution function (E-RDF) plots and energies for eight initialised and final structures of icosahedral $\text{Ag}_{205}\text{Au}_{104}$. The panels (a)-(h) are ordered from lowest to highest.

To demonstrate the robustness of the policy-based optimization of elemental ordering against random initialization, we analyze eight final structures optimized by the agent from distinct random initializations of the icosahedral $\text{Ag}_{205}\text{Au}_{104}$ (Figure 4). $\text{Ag}_{205}\text{Au}_{104}$ has a verifiably optimal "onion-shell"-like ground state ordering under the EMT potential [11]. This structure, which was also found by

agent (see Figure 3e), has alternating layers of Ag and Au, starting with a central Ag atom, and thus has an easily recognizable signature in the elemental radial distribution function (E-RDF) plots. In Figure 4a-h, we order the eight solutions found by the agent from different random initializations from the lowest final energy (best) (Figure 4a, which is that of the configuration in Figure 3e) to the highest final energy (worst). The E-RDF for the randomized initial configurations (left) and for the agent’s final structure (right) show that in all cases the agent recovers the shell structure despite varied initialisations, and the energy gaps between Figure 4a and the others are negligible ($\approx 10^{-5}$ meV/atom). The sole outlier (the worst structure, Figure 4h) reflects sub-optimal relaxation, and the energy delta is ≈ 0.1 meV/atom to Figure 4a, yet the elemental ordering and E-RDF remain visually identical. For the nanoparticle considered here, the RL-optimized structures recover the correct elemental occupation of the outer-shell sites, so the catalytically relevant surface motifs are consistent with those of the corresponding reference ground-state structures.

Computational cost The computational cost during both training and deployment comes mainly from the number of swap-relax operations and the typical number of L-BFGS steps per relaxation. The overall cost is dominated by these repeated relaxations rather than by policy inference. In the present setup, intermediate relaxations are capped at 100 L-BFGS steps and typically require about 15–20 steps in practice. For the 309-atom training case, the nominal budget corresponds to 7800 training structures with a horizon of 309 swap-relax steps per structure, with 2.4 million swap-relax operations during training (Figure 6). However, this setup was not computationally optimized. For binary nanoparticles, the useful horizon during training and deployment should in principle, be limited by the number of atoms of the smaller stoichiometric component, which for the most balanced 309-atom system $\text{Ag}_{155}\text{Au}_{154}$, would imply a maximum useful horizon of about 154 and an average useful horizon of about 77 when considering all compositions. During deployment, we observe that the structures converge on optimal ordering much earlier than the full horizon length N , e.g. after 165 swap-relax steps (Figure 8). Considering that the number of swaps to achieve correct ordering during deployment is roughly 1/4 of the horizon we employ now (Figure 8), the horizon could be shortened, thus reducing the training cost substantially, potentially to $\sim 100,000$ swap-relax operations with a more optimized protocol. During training we observe that the agent only needs roughly 1/6 of the current horizon to achieve correct ordering.

3.2 Policy generalisation allows extrapolation to different-sized NP (Experiment-2)

Extending the success of the model in generalizing over alloy compositions, the next step towards achieving a universal alloy NP structure solver is size generalization and extrapolation capabilities of the policy to unseen-sized NP motifs.

Training To test whether the agent’s policy can learn size-invariant ordering rules for icosahedral NP, we train on $\text{Ag}_X\text{Au}_{N-X}$ nanoparticles with $N \in \{55, 147, 561\}$ while *excluding* $N = 309$ NPs during the training process. We then evaluate the agent’s ability to resolve the lowest energy structure of 309-atom NPs. For consistency of comparison, we check the structures for the same eight Ag-Au compositions (ico-1 to ico-8 in Figure 5) as described in the previous section taken from Larsen et al. [11].

Results Comparing the energies of 309 atom NPs (ico-1 to ico-8) optimized with the policy from experiment 1 (trained with 309 atom NPs) against the same NPs optimized with the policy from this experiment (never seen 309 atom NPs during training) provides a benchmark of the model’s capability in size extrapolation. Figure 5 shows that deploying the policy for unseen sized NP optimization leads to a slight increase in the energy of the most stable structure found in some cases. The mean ΔE between the minimum energy structures from these two policies across systems is ≈ 0.021 eV (see Table 1). The robustness of finding the lowest energy structure when optimizing from different starting points is also preserved when extrapolating to 309 atom NP, similar to experiment 1. These results indicate that the learned policy can be reliably transferred across icosahedral shell counts when the alloying elements are consistent.

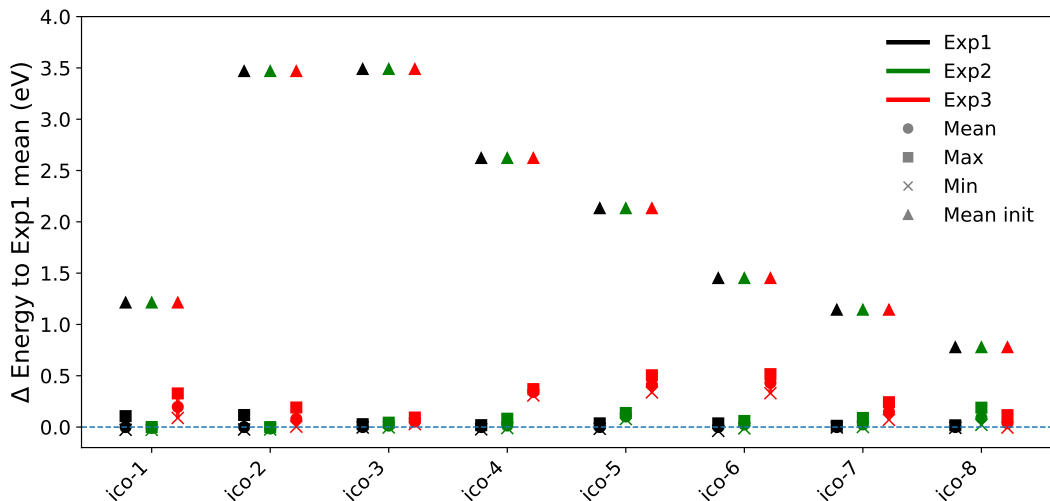


Figure 5: For all eight 309 atom test systems (ico-1 to ico-8), the summary of energies is shown as ΔE relative to the average energy of the final optimised structures from eight runs with policy from experiment 1 (dashed line). For each system, we depict the mean energy of the randomly initialised structure; the mean, maximum and minimum energies after optimisation of the structures from all runs. The dashed line at 0 denotes the baseline mean optimised structure energy from experiment 1. Optimisation runs from experiment 2 remain consistent and close to the results obtained in experiment 1. Experiment 3 results show that the policy trained with NPs of multiple element combinations fails to resolve the lowest energy structures in the size extrapolation situation. e.g. for ico-5 and ico-6 the outcomes from different optimisation runs are consistently more than 0.3eV higher in energy than structures found in experiment 1.

System	E2 Δ Avg	E2 Δ Best	E2 Δ Worst	E3 Δ Avg	E3 Δ Best	E3 Δ Worst	Exp1 spread
ico-1	-0.010	0.000	-0.106	0.196	0.115	0.222	0.133
ico-2	-0.014	-0.000	-0.118	0.079	0.028	0.073	0.141
ico-3	0.014	0.000	0.015	0.053	0.033	0.065	0.032
ico-4	0.015	0.012	0.063	0.342	0.330	0.351	0.040
ico-5	0.103	0.095	0.101	0.412	0.355	0.468	0.053
ico-6	0.025	0.025	0.024	0.431	0.367	0.480	0.073
ico-7	0.026	0.005	0.077	0.148	0.074	0.230	0.016
ico-8	0.091	0.029	0.172	0.037	0.002	0.099	0.024
Mean	0.031	0.021	0.028	0.212	0.163	0.248	0.064

Table 1: For each of the eight test 309 atom alloy nanoparticles, the average, lowest and highest energy(eV) after optimisation in experiment 2 (E2) and experiment 3 (E3) is reported relative to the average, lowest and highest energy after optimisation in experiment 1. The maximum to minimum energy range (Exp1 spread) of the final state indicates intrinsic variability within multiple runs for a specific NP case (ico-1 to ico-8).

3.3 Limited effectiveness in size extrapolation for cross-chemistry generalised policy (Experiment-3)

A model that can generalize among many different alloy elements and extrapolate to different sized NP can essentially be used to build foundational NP structures solvers that can be deployed across all elements and NP sizes.

Training To test the possibility of achieving multi-element generalization and size extrapolation jointly, we added a second bimetallic chemistry during training and checked for robustness and transferability. We trained on both Ag–Au and Pt–Ni for NP sized $N \in \{55, 147, 561\}$, while

excluding $N = 309$, and the policy was evaluated on the eight Ag–Au 309-atom NP as in the previous two experiments. We show training curves in Figure 7 in Appendix B.

Results Introducing Pt-Ni and Ag-Au together in training makes the policy less reliable in finding the optimal structure of unseen 309-atom NPs. Energies of the final optimized structure proposed by this policy trend are noticeably higher than those of experiments 1 or 2 (Figure 5). On average, the mean energy of optimized structures increases by ≈ 0.21 eV between systems, with the largest deviations observed for *ico-5* and *ico-6*. Even considering the most stable optimized structure from each system, the optimized energy increases by ≈ 0.16 eV. Some systems remain less affected (e.g., *ico-8*), but the optimized NP energy is consistently worse than in experiment 1 and is therefore unreliable for optimization of the NP structure. This points to a chemistry-induced distribution shift: mixing chemistries with distinct ordering energetics biases the policy away from Ag-Au motifs that were optimal in experiment 1. For PtNi nanoparticles, the jointly trained policy recovers chemically sensible orderings that agree qualitatively with prior literature [45], in particular the Pt-rich outer shell, although some discrepancies remain in the inner-shell arrangement. In particular, the RL framework reproduces key characteristics of the $\text{Ni}_{113}\text{Pt}_{196}$ and $\text{Ni}_{419}\text{Pt}_{50}$ nanoparticles reported previously [8], especially for the outer shells, where the Pt-rich surface structure is recovered correctly. The main discrepancies appear in the inner shells (Figure 9).

3.4 Robustness of inference

With Figure 5 we intended to assess the robustness and consistency of the three training setups across repeated optimizations from random initial chemical orderings, rather than only their single best-case performance. For this reason, the final energies are plotted relative to the average energy of the eight optimized runs for each experiment. In experiments 1 and 2, the optimized structures converge essentially to the same final ordering, and the small residual energy differences arise mainly from minor numerical variations in the L-BFGS relaxation (~ 0.01 meV) rather than from physically distinct chemical orderings or structures. By contrast, experiment 3 exhibits a larger spread in final energies and more frequent failure to recover the lowest-energy ordering, indicating reduced robustness and consistency in the multi-chemistry setting. A comparison to the lowest-energy structure is the more natural metric for benchmarking a global optimizer; this coincides with the baseline marker. For experiments 1 and 2, the near-identical final energies across repeated runs already indicate that the final structure reaches the global optimum but for experiment 3, a cumulative success-rate analysis may be more informative if there are lower energy variants encountered during the swap-relax steps.

4 Discussion

In this work, we have shown that, utilizing a molecular graph representation, an RL agent can reproduce provably optimal ground state nanoparticle orderings. The agent finds these orderings for varying compositions and can converge on identical optimal solutions from differently ordered initialisations of the same chemical composition. The proposed architecture and training scheme allow for successful deployment of the agent for NPs that have a different size than training NPs, but this size extrapolation is not robust if multiple different element combinations must be tackled with the same policy.

In the future, this RL framework needs to be further developed to enable generalization to larger combinatorial spaces, encompassing more atoms, atomic species, and other nanoparticle motifs and morphologies. The wider chemical space of NPs remain beyond the reach of traditional methods such as genetic algorithms, Monte Carlo, basin hopping and minimum integer programming. Compared with these classical optimization approaches the present RL method has a higher upfront training cost but offers the possibility of cost amortization across many related optimization problems. Classical methods typically require a fresh search for each new nanoparticle size or composition, whereas a trained RL policy can be reused and can reach low-energy orderings using relatively few additional swap-relax steps during deployment. We therefore do not claim that the present approach is a universal replacement for established methods in single-instance optimization, but rather that it becomes attractive when a broad family of related chemical-ordering problems must be solved repeatedly. However, it is worth noting that RL methods can also benefit from efficient search strategies developed for these classical approaches. In particular, symmetry-constrained search has proven highly effective in genetic-algorithm-based nanoparticle optimization by drastically reducing

the accessible ordering space while retaining chemically relevant low-energy motifs [8]. This suggests that symmetry-constrained RL could also be a promising approach to improve efficiency for highly symmetric nanoparticle motifs, for example by restricting actions to symmetry-inequivalent sites or groups. The search cost scales superlinearly while the objective landscape grows more complex. With RL, we hope to amortize exploration by learning transferable action priors and value estimates that can guide sampling toward high-yield regions with potentially fewer energy calls than naive search.

On the implementation side, the currently used frozen ORB-v3 backbone is a pragmatic choice, but its pretraining emphasizes crystalline bulk datasets (e.g. MPtraj, Alexandria) rather than nanoparticles. Although the architecture supports non-periodic systems, nanoparticle or surface-specific data are missing in the training set. Future iterations of our agent could thus benefit from, e.g., nanoparticle-trained interatomic potentials and/or from performing end-to-end fine-tuning of the encoder jointly with the policy/value heads on NP data. A complementary direction is to replace expensive per-step relaxations with learned relaxations. The present model extends earlier on-lattice periodic alloy ordering RL framework to nanoparticle alloy ordering, in addition also implicitly accounting for the effect of local distortions through structure relaxation during training. In principle, one might consider training a policy that learns both atomic swaps and explicitly performs lattice distortions toward low-energy structures, but this would introduce a much larger continuous action space associated with the displacement of all atomic positions and is therefore left for future work. Although the present environment is restricted to pair swaps to maintain a tractable action space and a well-defined per-step reward, the framework can in principle be extended to multi-atom moves through cyclic k-atom permutations, learned multi-swap actions, or hierarchical action policies, at the cost of a substantially larger action space and more difficult credit assignment. In Figure 3, we observed that in the final proposed structure from RL, a few atoms can be placed sub-optimally compared to the ideal solution. One reason for this could be that we currently have no mechanism to prevent energy-increasing moves late in the episode because same-species swaps are explicitly prohibited by masking. In practice, the agent thus currently learns to keep swapping atoms back and forth between the same positions in an attempt to maintain an optimal structure. This is not ideal, so an improvement to our method could be to implement a mechanism to avoid forcing non-productive moves. Accordingly, we will experiment with the removal of the same-species mask and introduce either a no-operation/stop action or a variable-length horizon. The latter could be implemented by introducing a per-step penalty to discourage unnecessary swaps. Together these changes might let the agent preserve the already optimal structures, anticipate relaxation effects, and generalize better as we expand our model to include more elements, nanoparticle sizes, and motifs.

5 Data availability statement

The codebase for this work is openly available at <https://github.com/Jote1s/medusa>.

6 Acknowledgments

We received funding from DNRF for the Pioneer Center for Accelerating P2X Materials Discovery (CAPEX) grant number P3, from the Det Frie Forskningsråd for Project “Data-driven quest for TWh scalable Na-ion battery (TeraBatt)” (2035-00232B) and “Autonomous agents of Discovery for earth-Abundant Na-ion battery cathodes (ADANA)” (3164-00297B). We also thank the Novo Nordisk Foundation Data Science Research Infrastructure 2022 Grant: A high-performance computing infrastructure for data-driven research on sustainable energy materials, Grant no. NNF22OC0078009.

A Algorithm details

Below, we detail the algorithm and implementation choices we have made. A graphical overview of the method is provided in Figure 2.

A.1 MDP and rewards

Each episode is a finite-horizon MDP

$$\mathcal{M} = (\mathcal{S}, \mathcal{A}, P, r, H, \gamma),$$

over a 309-atom icosahedral nanoparticle with a fixed random composition $\text{Ag}_x\text{Au}_{309-x}$ and randomly initialized ordering/positions. Here \mathcal{S} is the state space, \mathcal{A} the discrete action space, $P : \mathcal{S} \times \mathcal{A} \rightarrow \Delta(\mathcal{S})$ is the transition kernel $P(s'|s, a)$, $r : \mathcal{S} \times \mathcal{A} \times \mathcal{S} \rightarrow \mathbb{R}$ is the reward function, $H \in \mathbb{N}$ is the episode length, and $\gamma \in [0, 1]$ is the discount. In our environment, the transition $s_{t+1} \sim P(\cdot|s_t, a_t)$ is the *swap+relaxation* step (see Figure 1). In our setup, this transition is approximately deterministic. E_t is the potential energy after step t , and E_0 is the initial energy of the randomized configuration of the nanoparticle. With per-step relaxation, we define the instantaneous reward

$$r_t = E_{t-1} - E_t, \quad t = 1, \dots, H. \quad (2)$$

Because we do not use a discount factor for our rewards, *i.e.* $\gamma = 1$, the telescoping property holds exactly for our setup:

$$G = \sum_{t=0}^{H-1} r_t = \sum_{t=0}^{H-1} (E_t - E_{t+1}) = E_0 - E_1 + E_1 - E_2 + \dots + E_{T-1} - E_T = E_0 - E_H, \quad (3)$$

so maximizing undiscounted return is equivalent to minimizing final energy. We interface with the nanoparticle using the Atomic Simulation Environment (ASE) [46], and similarly compute energies in ASE.

For these calculations, we use the Effective Medium Theory (EMT) potential implemented in ASE [38, 47]. EMT is a semi-empirical tight-binding/second-moment-type model in which the total energy decomposes into a short-ranged repulsive pair term plus an embedding contribution that depends on a locally accumulated electron density from neighbours. Both contributions are modeled by decaying exponentials with element-specific parameters fitted to reproduce bulk lattice constants, cohesive energies, bulk moduli and vacancy formation energies of the pure elements. Heteronuclear (alloy) interactions follow the standard EMT mixing rules implemented with the same parameter set. These parameters are fitted to reproduce experimental and Density Functional Theory (DFT) data for the elemental metals Ni, Cu, Ag, Au, Pd, Pt and bimetallic alloys [38]. EMT thus captures the correct trends in relative stabilities of different configurations, such as the energetic ordering of alloy structures or cluster isomers [4]. In practice we use the compiled ASAP implementation, which provides a vectorized neighbor-list kernel in C/C++ with OpenMP parallelism. Since we work with nanoparticles, we disable periodic boundary conditions and add 10 Å of vacuum so that EMT’s short cutoff does not couple periodic images.

To perform local relaxations, we use the line-search L-BFGS optimizer [48] implemented in ASE. We use a maximum-force parameter f_{max} to decide when to stop the relaxation $\max_i \|\mathbf{F}_i\|_{\infty} \leq f_{\text{max}}$ or alternatively when a step budget N_{Max} is reached. In practice we use small relaxations at intermediate steps ($f_{\text{max}} = 0.01$, $N_{\text{Max}} = 100$) and a stricter final relaxation at $t = H$ ($f_{\text{max}} = 5 \times 10^{-3}$, $N_{\text{Max}} = 1000$). The reward is the energy drop after the *swap+relax* step has taken place.

A.2 State encoding and factorized policy

At time step t , the state s_t is the current nanoparticle (symbols and positions), which we encode using a pretrained ORB-v3 encoder [37]. This yields per-atom embeddings $\mathbf{h}_i \in \mathbb{R}^{D_0}$ for atom i . The action is a swap $a_t = (i_t, j_t)$ between an *anchor* index i_t and a *partner* index j_t . We parameterize the joint policy by a factorization

$$\pi_{\theta}(a_t | s_t) = \pi_{\theta_a}(i_t | s_t) \pi_{\theta_p}(j_t | s_t, i_t), \quad (4)$$

with $\theta = (\theta_a, \theta_p)$.

Time embedding. We make the policy explicitly time-aware by concatenating a fixed, non-learned positional code of the current step and a scale indicator of the episode length. Let $t \in \{0, \dots, H-1\}$ denote the step index and H the horizon. We define

$$\psi(t, H) = [PE(t), \log H] \in \mathbb{R}^{d+1},$$

where $PE(t) \in \mathbb{R}^d$ is the sinusoidal code

$$PE_{2m}(t) = \sin\left(\frac{t}{10000^{2m/d}}\right), \quad PE_{2m+1}(t) = \cos\left(\frac{t}{10000^{2m/d}}\right), \quad m = 0, \dots, \frac{d}{2} - 1.$$

The inclusion of $\log H$ conditions the policy on the remaining budget. While we use fixed horizons due to the fixed particle size, we aim to use this to promote transfer across tasks with different horizons in future implementations where particle sizes and motifs vary. In implementation, $\psi(t, H)$ is tiled to all atoms so that each per-atom feature vector at time t carries identical temporal context. In theory, this design breaks step-exchange symmetry (action preferences near the end of an episode may differ from those early on).

Anchor head. Let $\mathbf{h}_i \in \mathbb{R}^{D_0}$ be the per-atom embedding from the pretrained ORB-v3 encoder for atom i . The ORB-v3 encoder also outputs an $\ell = 1$ vector channel $\mathbf{v}_i \in \mathbb{R}^3$, which is a predicted force per atom. In our implementation, we recognize that the ORB-v3 model is not tailored to nanoparticles, and thus the predicted forces \mathbf{v}_i are not used directly to, e.g., relax the structure, but only used as force/dispersion "proxies", whose relation (if any) to the optimal ordering is learned inside the policy networks. To produce the anchor policy distribution, we compress this force proxy to a rotation-invariant scalar $\|\mathbf{v}_i\|_2$ and map it through a small MLP to obtain $\chi_i \in \mathbb{R}^{d_x}$. We provide χ_i to the agent in order to incentivize toward atoms with large local directional signal (high stress/instability), while $\|\mathbf{v}_i\|_2 = \|R\mathbf{v}_i\|_2$ for any $R \in \text{SO}(3)$ ensures frame-invariant logits. The time-aware anchor features are

$$\phi_i^{(a)}(t) = [\mathbf{h}_i, \chi_i, \psi(t, H)] \in \mathbb{R}^{D_0+d_x+(d+1)}. \quad (5)$$

An MLP $g_{\theta_a} : \mathbb{R}^{D_0+d_x+(d+1)} \rightarrow \mathbb{R}$ produces a scalar logit for each atom,

$$z_i^{(a)} = g_{\theta_a}(\phi_i^{(a)}(t)), \quad (6)$$

and the anchor distribution over indices $\{1, \dots, N\}$ is the categorical

$$\pi_{\theta_a}(i | s_t) = \text{softmax}(z^{(a)})_i \quad \text{with} \quad z^{(a)} = (z_1^{(a)}, \dots, z_N^{(a)}). \quad (7)$$

We do not rule out any atoms at the anchor stage (all atoms may serve as anchors). Instead, any masking is deferred to the partner head. Computationally, the anchor pass is $O(N)$ and $\psi(t, H)$ is broadcast to all atoms at step t .

Partner head (conditional on i). Given a sampled anchor i , we concatenate to each candidate partner atom indexed by j the embedding \mathbf{h}_j and the broadcast anchor embedding \mathbf{h}_i . We also augment the partner candidate features with two E(3)-invariant pairwise descriptors:

$$d_{ij} = \|x_j - x_i\|_2, \quad a_{ij} = \mathbf{v}_i^\top \mathbf{v}_j, \quad (8)$$

where d_{ij} is a radial separation and a_{ij} is a force-alignment term derived from the encoder's force predictions. Similar to the anchor features, the relation to the force-alignment term is learned, and the forces are not used directly. These two terms thereby inject a lightweight physics prior, allowing the policy to learn a signed preference (favor or penalize) for near-field swaps conditioned on these descriptors, while keeping the logits frame-invariant. The full partner features are therefore

$$\phi_{j|i}^{(p)}(t) = [\mathbf{h}_j, \mathbf{h}_i, \bar{\mathbf{e}}_{i \rightarrow j}, d_{ij}, a_{ij}, \psi(t, H)], \quad (9)$$

passed through an MLP g_{θ_p} to produce logits $z_j^{(p,i)} = g_{\theta_p}(\phi_{j|i}^{(p)})$. Feasibility is enforced by a masked categorical

$$\pi_{\theta_p}(j | s_t, i) = \text{softmax}(z^{(p,i)} + \mathbf{m}_{s_t, i})_j, \quad \mathbf{m}_{s_t, i}(j) = \begin{cases} -\infty, & Z_j = Z_i, \\ 0, & \text{otherwise,} \end{cases} \quad (10)$$

which prohibits same-species swaps and (therefore) self-swaps, which has the added effect of reducing the effective action space while preserving correct invariances of the logits.

Critic and value pooling. The value function $V_\phi(s_t)$ shares the time-aware per-atom inputs with the anchor head. We compute two permutation-invariant summaries of the per-atom features $\{h_i(t)\}_{i=1}^N$: a feature-wise attention pool $p^{(1)}$ and a uniform mean $p^{(2)}$. Let $a(h_i) \in \mathbb{R}^D$ be the output of a learned scoring MLP applied to h_i . For each feature channel d ,

$$W_{i,d} = \frac{\exp(a_d(h_i))}{\sum_{k=1}^N \exp(a_d(h_k))}, \quad p_d^{(1)} = \sum_{i=1}^N W_{i,d} h_{i,d}, \quad (11)$$

and

$$p^{(2)} = \frac{1}{N} \sum_{i=1}^N h_i. \quad (12)$$

Two MLP heads produce scalars $v_1 = v_{\phi_1}(p^{(1)})$ and $v_2 = v_{\phi_2}(p^{(2)})$. The final value is a gated sum

$$V_\phi(s_t) = \sigma(w_1) v_1 + \sigma(w_2) v_2, \quad \phi = (\phi_1, \phi_2),$$

where $w_1, w_2 \in \mathbb{R}$ are learnable scalars updated by backprop through the value loss and $\sigma(\cdot)$ is the logistic sigmoid. This dual value network strategy is inspired by twin-critic architectures [49, 50] in which two value estimators are trained in parallel. Their outputs are combined via a learnable weighted sum, providing lower bias and improved stability compared to a single critic. This is conceptually related to Double Q-learning and Clipped Double Q-learning, but differs in that we learn the aggregation weights rather than fixing them.

A.3 GAE and bootstrapping

We collect trajectories until a target number of complete episodes is reached. Let $d_t \in \{0, 1\}$ be the terminal flag ($d_t = 1$ if s_{t+1} is terminal). Define temporal difference (TD) residuals

$$\delta_t = r_t + \gamma(1 - d_t) V_\phi(s_{t+1}) - V_\phi(s_t), \quad (13)$$

and generalized advantages (GAE) [40] with parameter $\lambda \in [0, 1]$, truncated at episode ends,

$$\hat{A}_t = \sum_{\ell \geq 0} (\gamma\lambda)^\ell \left(\prod_{m=0}^{\ell-1} (1 - d_{t+m}) \right) \delta_{t+\ell}, \quad \hat{R}_t = \hat{A}_t + V_\phi(s_t). \quad (14)$$

Equivalently, the backward recursion $\hat{A}_t = \delta_t + \gamma\lambda(1 - d_t)\hat{A}_{t+1}$ with $\hat{A}_T = 0$. We normalize $\{\hat{A}_t\}$ per episode.

At each step t we append a record $\tau_t = (A_t, i_t, j_t, r_t, d_t, t, H, \log \pi_{\text{old}}^{(a)}(i_t | s_t), \log \pi_{\text{old}}^{(p)}(j_t | s_t, i_t), V_{\phi, \text{old}}(s_t))$, where S_t is the state before the swap, (i_t, j_t) is the sampled (anchor, partner), r_t the reward, $d_t \in \{0, 1\}$ the terminal flag, (t, H) reconstruct the time code, $\log \pi_{\text{old}}^{(a)}, \log \pi_{\text{old}}^{(p)}$ are the detached headwise log-probs under the behavior policy, and $V_{\phi, \text{old}}(s_t)$ the detached critic value. We also cache the joint old log-prob $\log \pi_{\text{old}} = \log \pi_{\text{old}}^{(a)} + \log \pi_{\text{old}}^{(p)}$. After collecting a target number of complete episodes, we compute (\hat{A}_t, \hat{R}_t) and, during PPO updates, re-encode each stored \hat{A}_t with the current networks to obtain current logits/entropies, rebuild the same mask from atomic numbers, reconstruct $\psi(t, H)$ from (t, H) , and form the current joint log-prob $\log \pi_\theta = \log \pi_\theta^{(a)} + \log \pi_\theta^{(p)}$ used in the importance ratio and KL gate.

A.4 PPO objectives and loss

Given the factorized policy of Equation (4), the joint log-probability used for training is

$$\log \pi_\theta(a_t | s_t) = \underbrace{\log \text{softmax}(\pi_{\theta_a}(i | s_t))}_{\text{anchor}} + \underbrace{\log \text{softmax}(\pi_{\theta_p}(j | s_t, i))}_{\text{partner}}. \quad (15)$$

Using the joint log-probability is necessary because the sampled action $a_t = (i_t, j_t)$ comes from a product distribution with a conditional partner head; equivalently,

$$\frac{\pi_\theta(a_t | s_t)}{\pi_{\theta_{\text{old}}}(a_t | s_t)} = \frac{\pi_{\theta_a}(i_t | s_t)}{\pi_{\theta_a^{\text{old}}}(i_t | s_t)} \cdot \frac{\pi_{\theta_p}(j_t | s_t, i_t)}{\pi_{\theta_p^{\text{old}}}(j_t | s_t, i_t)}. \quad (16)$$

With this, we define the importance ratio

$$\rho_t(\theta) = \frac{\pi_\theta(a_t | s_t)}{\pi_{\theta_{\text{old}}}(a_t | s_t)} = \exp \left(\log \pi_\theta(a_t | s_t) - \log \pi_{\theta_{\text{old}}}(a_t | s_t) \right). \quad (17)$$

Following PPO [39], we optimize the clipped surrogate

$$\mathcal{L}^{\text{CLIP}}(\theta) = \mathbb{E}_t \left[\min \left(\rho_t(\theta) \hat{A}_t, \text{clip}(\rho_t(\theta), 1 - \epsilon, 1 + \epsilon) \hat{A}_t \right) \right], \quad (18)$$

where $\epsilon > 0$ is the trust-region width and \hat{A}_t is the (per-episode normalized) generalized advantage estimate [40]. Here we have taken an ϵ -greedy strategy ($\epsilon = 0.05$). The clipping term is an unconstrained proxy for the trust-region penalty [51], limiting harmful updates when ρ_t deviates too far from 1 with $\hat{A}_t \neq 0$. We then combine the policy surrogate with a value regression and entropy regularization and minimize

$$\mathcal{J}(\theta, \phi) = -\alpha_{\text{pol}} \mathcal{L}^{\text{CLIP}}(\theta) + \alpha_{\text{vf}} \mathbb{E}_t \left[\ell_{\text{SmoothL1}}(V_\phi(s_t), \hat{R}_t) \right] - \alpha_{\text{ent}} \mathbb{E}_t \left[H(\pi_{\theta_a}(\cdot | s_t)) + H(\pi_{\theta_p}(\cdot | s_t, i_t)) \right], \quad (19)$$

with coefficients $\alpha_{\text{pol}}, \alpha_{\text{vf}}, \alpha_{\text{ent}} > 0$. Here $\hat{R}_t = \hat{A}_t + V_\phi(s_t)$ is the bootstrap target and ℓ_{SmoothL1} is the Huber loss [52], chosen for robustness to occasional large post-relaxation energy drops (heavy-tailed targets). Entropies $H(\cdot)$ are computed on the masked categoricals and encourage exploration in both heads [53, 54].

KL gating (early stopping). To further bound policy drift across PPO epochs, we monitor the empirical *joint* KL on each mini-batch,

$$\widehat{\text{KL}}(\pi_{\text{old}} \| \pi_\theta) = \mathbb{E}_t \left[\log \pi_{\text{old}}(a_t | s_t) - \log \pi_\theta(a_t | s_t) \right], \quad (20)$$

computed with Equation (15) over the masked feasible set. If $\widehat{\text{KL}} > c_{\text{stop}} \cdot \tau$ with $c_{\text{stop}} = 1.5$ and τ being a target max KL divergence (a hyperparameter set to 0.015 in our experiments), we stop the current PPO epoch early (break the mini-batch loop). This empirically prevents collapse and aligns with the trust-region motivation of TRPO/PPO [39, 51].

B Training curves

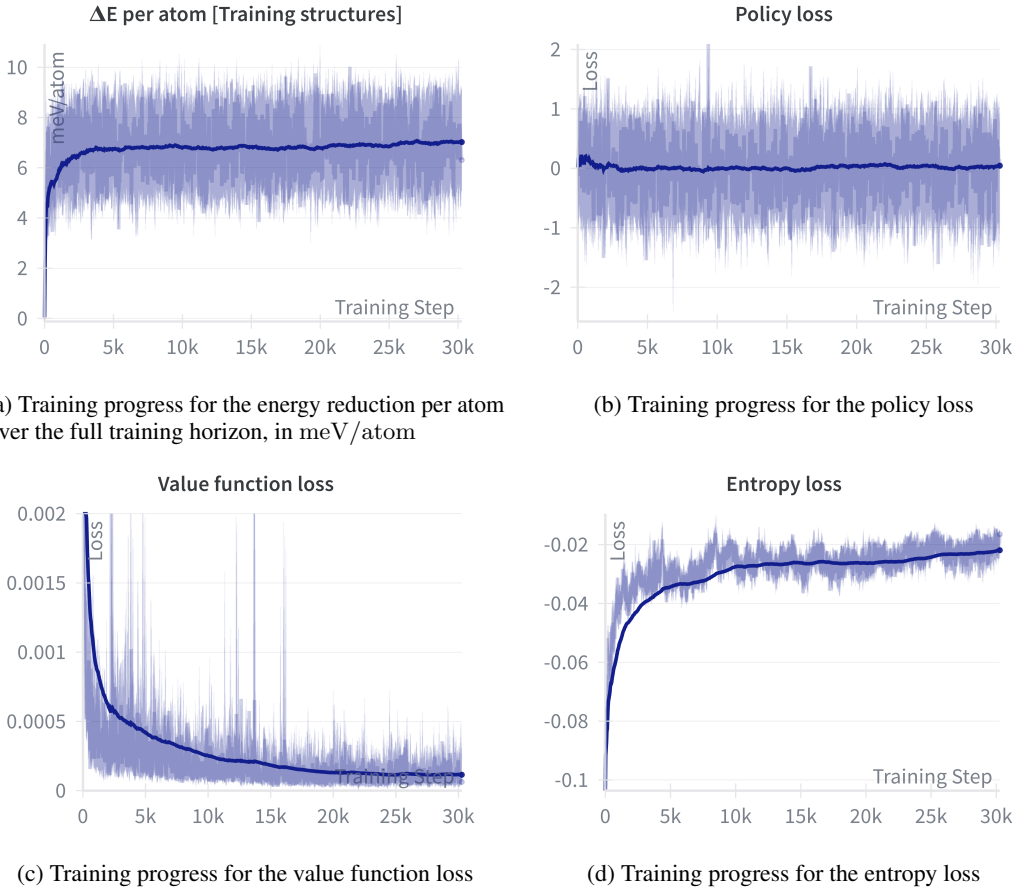
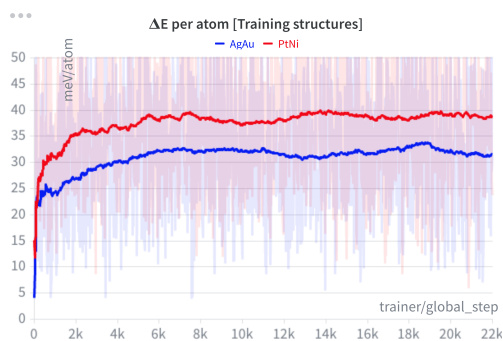


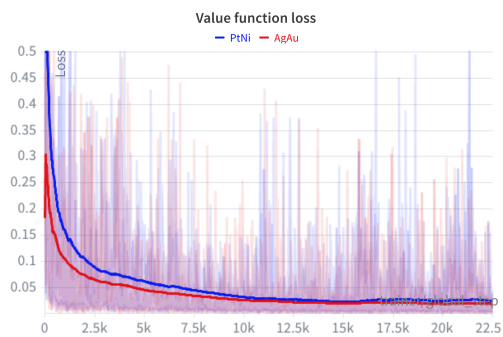
Figure 6: Training curves for our RL agent for Experiment 1. **(a)**: The pattern is typical for a well-posed PPO procedure, with return rising over time. In this case, we display the final energy reduction per atom, which is proportional to the return G , i.e. $\frac{\Delta E}{atom} = \frac{E_0 - E_H}{N_{atoms}} = \frac{G}{N_{atoms}}$ (see Equation 3). **(b)**: Since we use advantage normalization (GAE), the expectation value of the advantage \hat{A} is $\mathbb{E}[\hat{A}] \approx 0$, and near a local optimum the importance ratio (Equation 17) is $\rho_t \approx 1$, so the expected surrogate is near zero. Furthermore, clipping plus KL gating keeps ρ_t close to 1, which further dampens any trend. Finite-sample noise, changing data (on-policy), and alternating updates of policy/critic then produce batches where \mathcal{L}^{CLIP} is slightly positive or negative. Thus, the observed oscillation around 0 is expected. **(c)**: Meanwhile, the value loss falls because V_ϕ learns to match the bootstrap targets, shrinking TD errors over time. **(d)**: As the policy sharpens, the entropy $H(\pi)$ decreases as the policy becomes more exploitative.



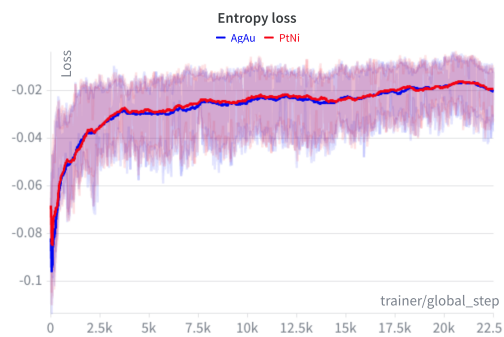
(a) Training progress for the energy reduction per atom over the full training horizon, in meV/atom



(b) Training progress for the policy loss



(c) Training progress for the value function loss



(d) Training progress for the entropy loss

Figure 7: Training curves for the RL agent for Experiment 3. The agent samples both AgAu and PtNi compositions, but we show the training here with separate curves for each type of system.

C Additional results

C.1 Full trajectory example

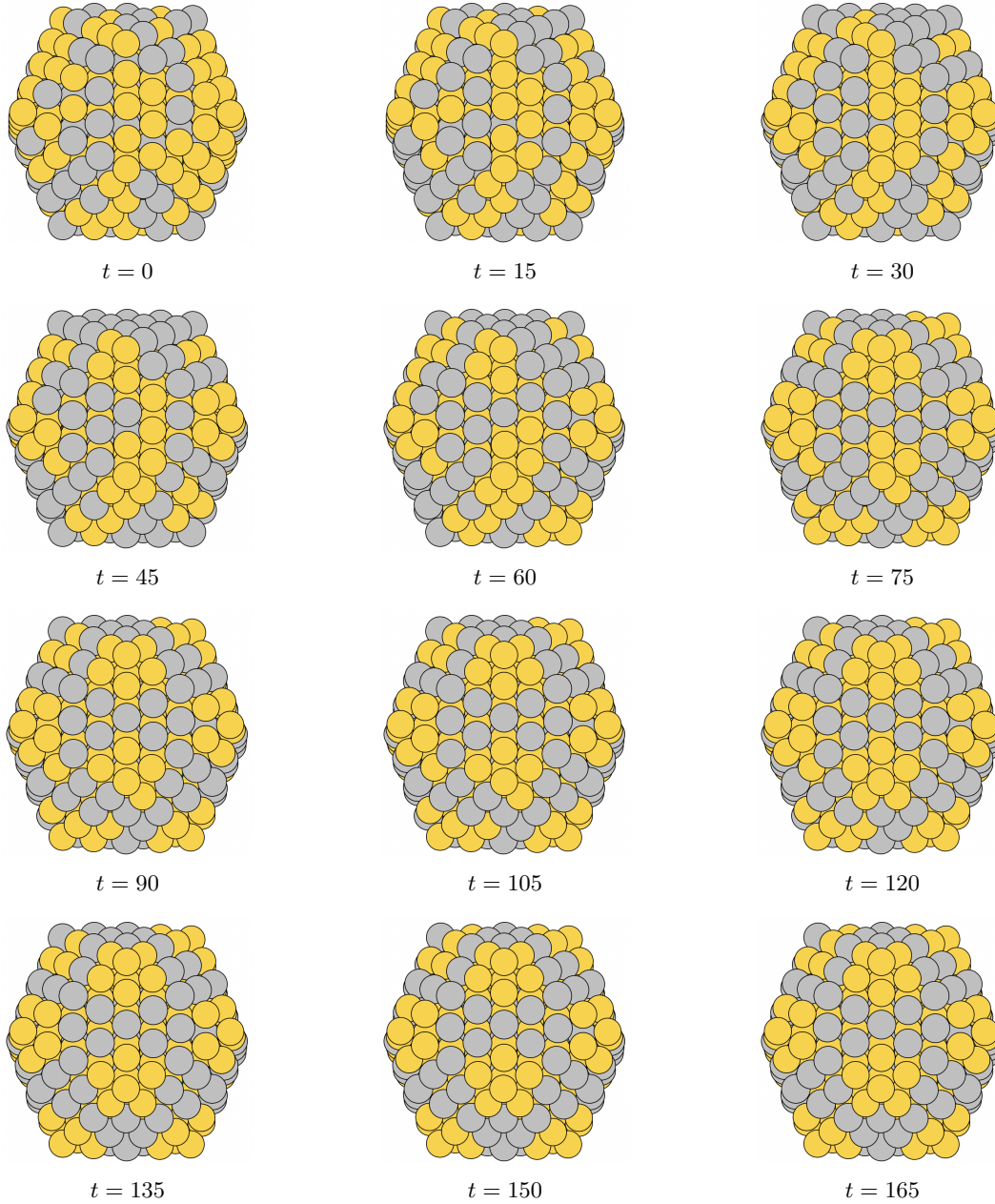


Figure 8: Snapshots from the first 165 steps (atomic swaps) for the best $\text{Ag}_{126}\text{Au}_{183}$ configuration found by the RL agent, which is equivalent to the provably optimal ordering found in [11]. As seen in the trajectory, most of the atoms in the final solution of Figure 3g are already in their final position at $t = 165$, even though the evaluation horizon is $H = 2 \times N_{atoms} = 618$. In particular, the top-left Ag atom is still out of place at $t = 165$ compared to Figure 3g, but the agent swaps this atom for Au around $t = 300$. All structures depicted in this figure are made with ASE [46].

C.2 Experiment 3 PtNi final structures

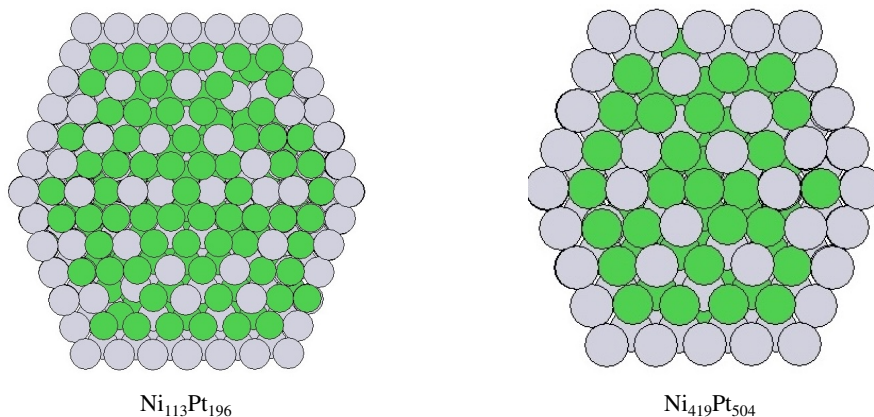


Figure 9: In Experiment 3, PtNi nanoparticle chemical orderings predicted by the jointly trained policy (AgAu and PtNi) are similar to the structures reported in the literature for $\text{Ni}_{113}\text{Pt}_{196}$ and $\text{Ni}_{419}\text{Pt}_{504}$ icosahedral nanoparticles. The RL model correctly recovers the Pt-rich outer shell in both cases, supporting that the jointly trained policy captures the physically expected surface segregation trend in PtNi nanoalloys, although there are discrepancies in the inner shell elemental ordering. Both structures depicted in this figure are made with ASE [46].

References

- [1] Neel Narayan, Ashokkumar Meiyazhagan, and Robert Vajtai. Metal nanoparticles as green catalysts. *Materials*, 12(21):3602, 2019.
- [2] Samantha M McIntyre and Anna L Garden. Computational modelling of nanoparticle catalysis. *Nanoscale*, 17(24):14491–14520, 2025.
- [3] Dennis Johan Loevlie, Brenno Ferreira, and Giannis Mpourmpakis. Demystifying the chemical ordering of multimetallic nanoparticles. *Accounts of Chemical Research*, 56(3):248–257, 2023.
- [4] Steen Lysgaard, David D Landis, Thomas Bligaard, and Tejs Vegge. Genetic algorithm procreation operators for alloy nanoparticle catalysts. *Topics in Catalysis*, 57:33–39, 2014.
- [5] N Zhang, FY Chen, and XQ Wu. Global optimization and oxygen dissociation on polyicosahedral Ag_3Cu_6 core-shell cluster for alkaline fuel cells. *Scientific reports*, 5(1):11984, 2015.
- [6] Manuella Cerbelaud, Riccardo Ferrando, Giovanni Barcaro, and Alessandro Fortunelli. Optimization of chemical ordering in agau nanoalloys. *Physical Chemistry Chemical Physics*, 13(21):10232–10240, 2011.
- [7] Fabio R Negreiros, Zdenka Kuntová, Giovanni Barcaro, Giulia Rossi, Riccardo Ferrando, and Alessandro Fortunelli. Structures of gas-phase ag–pd nanoclusters: a computational study. *The Journal of chemical physics*, 132(23), 2010.
- [8] Shuang Han, Giovanni Barcaro, Alessandro Fortunelli, Steen Lysgaard, Tejs Vegge, and Heine Anton Hansen. Unfolding the structural stability of nanoalloys via symmetry-constrained genetic algorithm and neural network potential. *npj Computational Materials*, 8(1):121, 2022.
- [9] Pablo Álvarez-Zapatero, A Vega, and A Aguado. A neural network potential for searching the atomic structures of pure and mixed nanoparticles. application to znmg nanoalloys with an eye on their anticorrosive properties. *Acta Materialia*, 220:117341, 2021.
- [10] Abhishek Ojha, Satya S Bulusu, Arup Banerjee, et al. Ann and dft investigation of 55-atom icosahedral ag-pt nanoalloys: Understanding structure, dynamics, and o₂ activation. *Computational and Theoretical Chemistry*, 1238:114691, 2024.
- [11] Peter Mahler Larsen, Karsten Wedel Jacobsen, and Jakob Schiøtz. Rich ground-state chemical ordering in nanoparticles: Exact solution of a model for ag-au clusters. *Physical Review Letters*, 120(25):256101, 2018.
- [12] Nongnuch Artrith and Alexie M Kolpak. Grand canonical molecular dynamics simulations of cu–au nanoalloys in thermal equilibrium using reactive ann potentials. *Computational Materials Science*, 110:20–28, 2015.
- [13] J Pirart, A Front, D Rapetti, C Andreazza-Vignolle, P Andreazza, C Mottet, and R Ferrando. Reversed size-dependent stabilization of ordered nanophases. *Nature Communications*, 10(1):1982, 2019.
- [14] Davide Bochicchio, Riccardo Ferrando, Rada Novakovic, Emanuele Panizon, and Giulia Rossi. Chemical ordering in magic-size ag–pd nanoparticles. *Physical Chemistry Chemical Physics*, 16(48):26478–26484, 2014.
- [15] AL Gould, CJ Heard, AJ Logsdail, and CRA Catlow. Segregation effects on the properties of (auag) 147. *Physical Chemistry Chemical Physics*, 16(39):21049–21061, 2014.
- [16] Daojian Cheng, Shuai Yuan, and Riccardo Ferrando. Structure, chemical ordering and thermal stability of pt–ni alloy nanoclusters. *Journal of Physics: Condensed Matter*, 25(35):355008, 2013.
- [17] Gustavo G Rondina and Juarez LF Da Silva. Revised basin-hopping monte carlo algorithm for structure optimization of clusters and nanoparticles. *Journal of chemical information and modeling*, 53(9):2282–2298, 2013.

- [18] Davide Bochicchio and Riccardo Ferrando. Morphological instability of core-shell metallic nanoparticles. *Physical Review B—Condensed Matter and Materials Physics*, 87(16):165435, 2013.
- [19] Fuyi Chen and Roy L Johnston. Energetic, electronic, and thermal effects on structural properties of ag- au nanoalloys. *ACS nano*, 2(1):165–175, 2008.
- [20] Nathan S Froemming and Graeme Henkelman. Optimizing core-shell nanoparticle catalysts with a genetic algorithm. *The Journal of chemical physics*, 131(23), 2009.
- [21] Steen Lysgaard, Jón SG Mýrdal, Heine A Hansen, and Tejs Vegge. A dft-based genetic algorithm search for aucu nanoalloy electrocatalysts for co 2 reduction. *Physical Chemistry Chemical Physics*, 17(42):28270–28276, 2015.
- [22] Domingos DC Rodrigues, Augusto M Nascimento, Hélio A Duarte, and Jadson C Belchior. Global optimization analysis of cunaum (n+ m= 38) clusters: Complementary ab initio calculations. *Chemical Physics*, 349(1-3):91–97, 2008.
- [23] Ji-ping Tao, Qing-shuang Ji, Gui-fang Shao, Ze-peng Li, Tun-dong Liu, and Yu-hua Wen. Stable structure optimization of pt-x-cu (x= au, ag, pd and rh) trimetallic nanoparticles. *Journal of alloys and compounds*, 716:240–250, 2017.
- [24] James Dean, Michael J Cowan, Jonathan Estes, Mahmoud Ramadan, and Giannis Mpourmpakis. Rapid prediction of bimetallic mixing behavior at the nanoscale. *ACS nano*, 14(7):8171–8180, 2020.
- [25] Tun-Dong Liu, Liang-You Xu, Gui-Fang Shao, Na-Na Tu, Ji-Ping Tao, and Yu-Hua Wen. Structural optimization of pt–pd–rh trimetallic nanoparticles using improved genetic algorithm. *Journal of Alloys and Compounds*, 663:466–473, 2016.
- [26] Arnaldo Rapallo, Giulia Rossi, Riccardo Ferrando, Alessandro Fortunelli, Benjamin C Curley, Lesley D Lloyd, Gary M Tarbuck, and Roy L Johnston. Global optimization of bimetallic cluster structures. i. size-mismatched ag–cu, ag–ni, and au–cu systems. *The Journal of chemical physics*, 122(19), 2005.
- [27] Mathias S Jørgensen, Henrik L Mortensen, Søren A Meldgaard, Esben L Kolsbjerg, Thomas L Jacobsen, Knud H Sørensen, and Bjørk Hammer. Atomistic structure learning. *The Journal of Chemical Physics*, 151(5), 2019.
- [28] Henrik Lund Mortensen, Søren Ager Meldgaard, Malthe Kjær Bisbo, Mads-Peter V Christiansen, and Bjørk Hammer. Atomistic structure learning algorithm with surrogate energy model relaxation. *Physical Review B*, 102(7):075427, 2020.
- [29] Søren A Meldgaard, Henrik L Mortensen, Mathias S Jørgensen, and Bjørk Hammer. Structure prediction of surface reconstructions by deep reinforcement learning. *Journal of Physics: Condensed Matter*, 32(40):404005, 2020.
- [30] Mads-Peter V Christiansen, Henrik Lund Mortensen, Søren Ager Meldgaard, and Bjørk Hammer. Gaussian representation for image recognition and reinforcement learning of atomistic structure. *The Journal of Chemical Physics*, 153(4), 2020.
- [31] Søren Ager Meldgaard, Jonas Köhler, Henrik Lund Mortensen, Mads-Peter V Christiansen, Frank Noé, and Bjørk Hammer. Generating stable molecules using imitation and reinforcement learning. *Machine Learning: Science and Technology*, 3(1):015008, 2022.
- [32] Nazir Ahmed, Muhammad Umar Farooq, and Fuyi Chen. Materials discovery through reinforcement learning: a comprehensive review. *AI & Materials*, 1(2):1–2, 2025.
- [33] Gregor Simm, Robert Pinsler, and José Miguel Hernández-Lobato. Reinforcement learning for molecular design guided by quantum mechanics. In *International Conference on Machine Learning*, pages 8959–8969. PMLR, 2020.
- [34] Jonas Elsborg and Arghya Bhowmik. Equivariant graph-representation-based actor–critic reinforcement learning for nanoparticle design. *Journal of Chemical Information and Modeling*, 63(12):3731–3741, 2023.

- [35] Daniel Flam-Shepherd, Alexander Zhigalin, and Alán Aspuru-Guzik. Scalable fragment-based 3d molecular design with reinforcement learning. *arXiv preprint arXiv:2202.00658*, 2022.
- [36] Jonas Elsborg and Arghya Bhowmik. Artisan: navigating the complexity of material structures with deep reinforcement learning. *Machine Learning: Science and Technology*, 5(3):035043, 2024.
- [37] Benjamin Rhodes, Sander Vandenhaute, Vaidotas Šimkus, James Gin, Jonathan Godwin, Tim Duignan, and Mark Neumann. Orb-v3: atomistic simulation at scale, 2025. URL <https://arxiv.org/abs/2504.06231>.
- [38] Karsten W Jacobsen, Per Stoltze, and JK Nørskov. A semi-empirical effective medium theory for metals and alloys. *Surface Science*, 366(2):394–402, 1996.
- [39] John Schulman, Filip Wolski, Prafulla Dhariwal, Alec Radford, and Oleg Klimov. Proximal policy optimization algorithms. *arXiv preprint arXiv:1707.06347*, 2017.
- [40] John Schulman, Philipp Moritz, Sergey Levine, Michael Jordan, and Pieter Abbeel. High-dimensional continuous control using generalized advantage estimation. *arXiv preprint arXiv:1506.02438*, 2015.
- [41] Riccardo Ferrando, Julius Jellinek, and Roy L Johnston. Nanoalloys: from theory to applications of alloy clusters and nanoparticles. *Chemical reviews*, 108(3):845–910, 2008.
- [42] Mohammad Molayem, Valeri G Grigoryan, and Michael Springborg. Global minimum structures and magic clusters of cu m ag n nanoalloys. *The Journal of Physical Chemistry C*, 115(45):22148–22162, 2011.
- [43] Mohammad Molayem, Valeri G Grigoryan, and Michael Springborg. Theoretical determination of the most stable structures of ni m ag n bimetallic nanoalloys. *The Journal of Physical Chemistry C*, 115(15):7179–7192, 2011.
- [44] Min Zhang and René Fournier. Structure of 55-atom bimetallic clusters. *Journal of Molecular Structure: THEOCHEM*, 762(1-3):49–56, 2006.
- [45] Juan Esteban Montoya Cardona, Antoine Salichon, Nathalie Tarrat, Emilie Gaudry, and David Loffreda. Structural, ordering, and magnetic properties of pt_ni nanoalloys explored by density functional theory and stability descriptors. *The Journal of Physical Chemistry C*, 127(36):18043–18057, 2023.
- [46] Ask Hjorth Larsen, Jens Jørgen Mortensen, Jakob Blomqvist, Ivano E Castelli, Rune Christensen, Marcin Dułak, Jesper Friis, Michael N Groves, Bjørk Hammer, Cory Hargus, et al. The atomic simulation environment—a python library for working with atoms. *Journal of Physics: Condensed Matter*, 29(27):273002, 2017.
- [47] Karsten Wedel Jacobsen, JK Nørskov, and Martti J Puska. Interatomic interactions in the effective-medium theory. *Physical Review B*, 35(14):7423, 1987.
- [48] Dong C Liu and Jorge Nocedal. On the limited memory bfgs method for large scale optimization. *Mathematical programming*, 45(1):503–528, 1989.
- [49] Hado Hasselt. Double q-learning. *Advances in neural information processing systems*, 23, 2010.
- [50] Hado Van Hasselt, Arthur Guez, and David Silver. Deep reinforcement learning with double q-learning. In *Proceedings of the AAAI conference on artificial intelligence*, volume 30,1, 2016.
- [51] John Schulman, Sergey Levine, Pieter Abbeel, Michael Jordan, and Philipp Moritz. Trust region policy optimization. In *International conference on machine learning*, pages 1889–1897. PMLR, 2015.
- [52] Peter J Huber. Robust estimation of a location parameter. In *Breakthroughs in statistics: Methodology and distribution*, pages 492–518. Springer, 1992.

- [53] Ronald J Williams. Simple statistical gradient-following algorithms for connectionist reinforcement learning. *Machine learning*, 8(3):229–256, 1992.
- [54] Volodymyr Mnih, Adria Puigdomenech Badia, Mehdi Mirza, Alex Graves, Timothy Lillicrap, Tim Harley, David Silver, and Koray Kavukcuoglu. Asynchronous methods for deep reinforcement learning. In *International conference on machine learning*, pages 1928–1937. PmLR, 2016.